In-situ frictional behavior of subducting sediment in the shallow Nankai Trough

Hanaya Okuda[1,2,*,†], Manami Kitamura[3], Miki Takahashi[4], Asuka Yamaguchi[1,2]

[1] Department of Ocean Floor Geoscience, Atmosphere and Ocean Research Institute, University of Tokyo, Japan

[2] Department of Earth and Planetary Science, University of Tokyo, Japan

[3] Research Institute of Geo-Resources and Environment, Geological Survey of Japan, National Institute of Advanced Industrial Science and Technology, Japan

[4] Research Institute of Earthquake and Volcano Geology, Geological Survey of Japan, National Institute of Advanced Industrial Science and Technology, Japan

[*] Corresponding author: Hanaya Okuda (h.okuda@jamstec.go.jp)

[†] Now at Kochi Institute for Core Sample Research (X-star), Japan Agency for Marine-Earth Science and Technology (JAMSTEC), Japan.

This is a non-peer reviewed preprint submitted to EPSL.

Abstract

The transition from smectite to illite at around the depth with temperature of ~150 °C has long been hypothesized as one of controlling factors of the updip limit depth of the seismogenic zone of subduction zones. Although illite has a higher friction coefficient than smectite, previous friction experiments have little reported that the smectite-illite transition accompanies the transition from velocity strengthening (not seismogenic) to velocity weakening (potentially seismogenic). In this study, we simulated *in-situ* temperature-pressure-mineral conditions along the shallow plate boundary in the Nankai Trough, and conducted friction experiments to further constrain the role of smectite-illite transition in seismogenesis in subduction zones. We found that friction coefficient of the simulated sediment increased with the progress of illitization and followed the Reuss average of friction coefficients of the mineral phases. The obtained friction coefficients and the Coulomb wedge model inferred that the pore pressure conditions around the plate boundary may be over-pressured but not as high as lithostatic pressure. Higher friction coefficients of sediment due to diagenetic processes will be required to sustain the nearly lithostatic pore pressure along the plate boundary. The velocity dependence of friction coefficient ($a-b$) was always positive except under the velocity conditions lower than ~10 μm/s at 171 °C. Therefore, the shallow slow earthquakes beneath the outer prism cannot be explained only by the frictional instability of unconsolidated sediment. Since the smectite-illite transition mostly completes at ~30 km landward from the trough axis, the transition from velocity strengthening to velocity weakening observed at 171 °C is caused by temperature-dependent frictional behavior of illite-rich material. Hence the updip limit depth of the seismogenic zone of subduction zones would be mainly controlled by frictional

properties of illite-rich material.

Keywords

Friction; Nankai Trough; Smectite-illite transition; Seismogenic zone; Slow earthquake; Subduction zone

1. Introduction

The seismogenic zone of subduction zones is the depth range where sources of megathrust earthquakes locate. Previous studies suggested that the seismogenic zone is limited by temperature such that the updip limit depth is equivalent to the depth where temperature is ~150 °C and the downdip limit is the depth with temperature of ~350 °C (Hyndman et al., 1997). This inference led the idea that material transitions occurring at those temperatures may control the updip/downdip limit depths. Smectite-illite (S/I) transition is one of the candidates that determine the updip limit depth of seismogenic zone because smectite turns into illite at around ~150 °C (Pytte & Reynolds, 1989), and smectite is abundant in (hemi)pelagic sediment subducting along the plate boundary (Vrolijk, 1990). Since smectite shows a quite low friction coefficient and illite has a higher friction coefficient, the transition from smectite into illite was considered to be able to accumulate more stress and possibly to lead to stick-slip behavior (Hyndman et al., 1997). However, stick-slip behavior is primarily controlled not by the frictional strength but by frictional instability of a material (Ruina, 1983). Therefore, the transition in frictional instability induced by the S/I transition must be examined to evaluate its role in the onset of seismogenesis in subduction zones.

Previous studies under room temperature showed that illite-rich gouge does not exhibit velocity-weakening behavior, which is requisite to induce frictional instability, at various effective normal stress, velocity, and shear strain conditions (Saffer & Marone, 2003). The stable friction of illite was also observed under water pressurized conditions with being mixed with quartz and smectite (Tembe et al., 2010). Experiments using marine core sediments from the Nankai Trough neither showed a transition from velocity strengthening to velocity weakening with increasing illite content in S/I mixed layers (Saffer et al., 2012). Those studies under room temperature barely supported the hypothesis that the transition from smectite to illite controls the transition in seismogenesis. In the cases of high temperature conditions, illite starts to exhibit velocity weakening at 150 °C when the system is dry (Kubo & Katayama, 2015) and at 200 °C when the system is hydrothermal (den Hartog et al., 2012). However, smectite also shows velocity-weakening behavior with increasing temperature (Kubo & Katayama, 2015; Mizutani et al., 2017); therefore, the mineralogical change may not necessarily contribute to the updip limit of seismogenic zone. Nevertheless, there have been few studies under hydrothermal conditions on the mixture of smectite and illite with varying illite content, which can further constrain the role of S/I transition in seismogenesis in shallow depths of subduction zones. In this study, we simulate the *in-situ* temperature-pressure-mineral conditions along the Kumano transect in the Nankai Trough, SW Japan, based on its geological and thermal structures coupled with the kinetics of S/I transition. Laboratory friction experiments on several points along the plate boundary were conducted under the *in-situ* conditions. The obtained results will be compared with observed seismic activities in the shallow part of the Nankai Trough, and the relationship between the S/I transition and seismogenesis will be discussed.

2. *In-situ* temperature-pressure-mineral conditions in the Nankai Trough

The Nankai Trough is one of the most studied convergent margins where the Philippine Sea plate subducts beneath the Amurian microplate (Figure 1a). Observations with dense seismic networks, borehole measurements, and GNSS-A measurements have found the shallow slow earthquakes along the plate boundary beneath the accretionary prism (Takemura, Baba, et al., 2022; Yokota & Ishikawa, 2020). Nankai and Tonankai megathrust earthquakes in 1946 and 1944 occurred at the seismogenic depths around the Kii peninsula (Ando, 1975; Garrett et al., 2016).

The Kumano transect locates offshore the Kii peninsula and has been broadly studied through the Nankai Trough Seismogenic Zone Experiment (NanTroSEIZE) project of the Integrated Ocean Drilling Program/International Ocean Discovery Program (IODP). The NanTroSEIZE project drilled 17 sites to collect sediment samples beneath the seafloor and to install borehole observatories. The Site C0002 on the Kumano forearc basin penetrated the inner accretionary prism down to over 3200 mbsf (meter below sea floor), and mineralogical analyses on cuttings samples from the Site C0002 captured the transition from smectite to illite (Underwood & Song, 2016). Previous studies (Hüpers et al., 2019) proposed a model implementing evolution of geological structure (Screaton et al., 1990), thermal structures (Figure 1b, Sugihara et al., 2014), and kinetics of the S/I transition (Pytte & Reynolds, 1989). In this study, we followed this model and obtained the *in-situ* temperature-pressure-mineral conditions along the plate boundary fault in the Nankai Trough (Figures 1b and c). Along the bottom of the accretionary prism, the S/I transition completed 90% at about 30 km landward from the trough axis (Figure 1c) where the temperature reaches 150 ℃ (Figure 1b). Illite content may be overestimated when the underthrusting is faster, or underestimated when the temperature is higher. Although such uncertainties may laterally shift the distribution of S/I, we will not consider them because the current model well-explains the S/I transition observed along the Site C0002 (see Hüpers et al. (2019) for details).

3. Methods

3.1. Materials and experimental conditions

According to the XRD measurements on the cuttings from the Site C0002 and the Site C0011 (input site on the Philippine Sea Plate), the mineral composition of sediments in the Nankai Trough approximately contain ~20% of quartz, ~20% of plagioclase, and ~60% of clay minerals (Tobin et al., 2015). Here we assume that this mineral composition is uniform within the prism and the incoming/underthrust sediment. We selected five locations along the bottom of the accretionary prism having illite fraction in S/I mixture of 30, 50, 70, 90, and 95% (Figure 1c), which corresponds to the temperature conditions of 55, 104, 118, 150, and 171 ℃, respectively (Figure 1b). We prepared 0.8 g of a gouge material (20 wt% of quartz, 10 wt% of albite, 10 wt% of orthoclase, and 60 wt% of S/I mixture) by crushing and sieving individual minerals to be less than 100 μm and then mixing them homogeneously. We noticed that the illite grain may contain ~10% of quartz; therefore, the gouge with high illite contents may have higher quartz contents. We accordingly calibrate its effect to interpret the experimental results (see section 5.1). Two porous alumina pistons (diameter = 20 mm, permeability ~ 10^{-16} m^2) with 30° sawcut, whose surfaces were roughened before an experiment by using carborundum (grit 80), were used to sandwich the gouge material. The gouge had an initial thickness of ~1.3 mm. As for pressure conditions, we assumed that the seafloor at the trough axis is 4300 m below sea level and calculated lithostatic and hydrostatic pressures at a given locations by the geological structure and densities of seawater (1.024 g/cm^3) and sediments (2.2 g/cm^3). See Table 1 for the experimental conditions at the five locations.

3.2. Experimental procedures

Friction experiments were conducted using the Ar-gas medium high-pressure-high-temperature triaxial deformation apparatus in Geological Survey of Japan (Masuda et al., 2002). The gouge and sawcut pistons were confined by polytetrafluoroethylene (PTFE) jacket and copper foil, and then assembled with pairs of tungsten-carbide (WC) and alumina spacers. The entire assembly was then sealed by PTFE jacket (Figure 2a). Two thermocouples were placed through holes of spacers to measure and control temperature near the sample. These holes were also used to introduce distilled water as pore fluid. Both Ar-gas and distilled water were independently pressurized and introduced to the pressure vessel and to the sample assembly by servo-controlled pressure intensifiers (Figure S1). Pore fluid volume was measured by the displacement of the piston in the pressure intensifier, and used to qualitatively see if the gouge dilates or compacts. Since the change in pore fluid volume during the compaction stage and at the beginning of the run-in stage was little (Figure 2b), we assume that compaction of porous alumina pistons can be ignored.

Once the sample assembly and a furnace were set in thet pressure vessel and load frame, we set the confining pressure (P_c) to the *in-situ* lithostatic pressure and the pore pressure (P_f) to the half of the *in-situ* hydrostatic condition. Then, the temperature was set to the *in-situ* condition. After the system was stabilized at the *in-situ* temperature, and *in-situ* P_c, and half of the *in-situ* hydrostatic P_f conditions, deformation was applied with 1 μm/s in the axial direction for the axial displacement of ~0.2-0.3 mm to yield the gouge (Figure 2b). Then the applied force was unloaded. After this load-unload sequence ("compaction stage"), we increased the P_f to the *in-situ* hydrostatic condition and resumed loading with the axial loading rate (V_{axial}) of 1 μm/s until the axial displacement reached 0.75 mm (~0.87 mm for the sliding displacement along the sawcut), namely the "run-in stage". Then we stepped V_{axial} to 0.1-0.01-0.1-1-10-100-10-100-10-1-0.1-0.01-0.1-1-10 μm/s with having ~0.06 mm of axial displacement for each step ("velocity step sequence") to investigate the velocity dependence of friction coefficient (Figure 2b). After the final step ended, we unloaded and decreased the temperature and pressures to ambient conditions without exceeding the *in-situ* effective pressure conditions. We conducted one additional experiment with five PTFE sheets sandwiched to determine the strength of PTFE jackets and copper foil around the sample. This jacket test was done at room temperature under the lowest effective stress condition (P_c = 16.1 MPa, P_f = 0 MPa) with V_{axial} = 1 μm/s. We assumed that the jacket strength depends only on displacement and that it is independent on pressure and temperature conditions because the jacket effect became relatively less significant for the experiments under higher effective stress conditions that simultaneously underwent higher temperature conditions. The measured jacket strength was subtracted from the force on the sample assembly.

3.3. Data processing

During experiments, temperature and pressure conditions, axial displacement, and differential stress were continuously logged with sampling rates of 0.2 (for the axial loading rate (V_{axial}) = 0.01 μm/s) to 250 Hz (for V_{axial} = 100 μm/s). Differential stress on the sample was calibrated using two data measured by external and internal load cells (Noda & Takahashi, 2016). As shear deformation was forced to occur along 30° sawcut, friction coefficient (μ) can be calculated as follows:

$$\mu = \frac{\sigma_{diff} \sin 2\varphi}{2\left(\sigma_{eff} + \sigma_{diff} \sin^2 \varphi\right)}, \qquad (6)$$

where σ_{diff} is differential stress after the jacket effect has been corrected, σ_{eff} is effective pressure (=P_c−P_f), and φ is the angle of shear plane from the loading axis (30° in this study).

For evaluating the contribution of each mineral phase on the friction coefficient of the gouge, we use the Reuss average:

$$\mu = \left(\sum_m \frac{r_m}{\mu_m}\right)^{-1}, \tag{7}$$

and the Voigt average:

$$\mu = \sum_m r_m \mu_m , \tag{8}$$

where r_m is a fraction of the material m, and μ_m is the friction coefficient for the mineral phase m (Moore & Lockner, 2011). In the system described by the Reuss average, all grains are subjected to identical stress, whereas all grains undergo identical strain in the system described by the Voigt average (Moore & Lockner, 2011).

At each velocity step, we fit the rate- and state-dependent friction (RSF) law to the experimental data to determine the RSF parameters. We used the single-state variable version of the RSF law:

$$\mu = \mu_0 + a \ln\left(\frac{V}{V_0}\right) + b \ln\left(\frac{V_0 \theta}{d_c}\right), \tag{9}$$

where V and V_0 are the sliding velocity after and before the velocity step, respectively, μ_0 is the steady state friction coefficient at V_0, a and b are non-dimensional parameters for the direct effect and the evolutionary effect, respectively, d_c is a characteristic slip displacement for the friction coefficient to become the steady state at V, and θ is a state variable following the slip law (Dieterich, 1979; Ruina, 1983):

$$\frac{d\theta}{dt} = -\left(\frac{V\theta}{d_c}\right) \ln\left(\frac{V\theta}{d_c}\right). \tag{10}$$

The ($a-b$) value for each velocity step was then calculated to see if the material can nucleate an earthquake or not. When ($a-b$) is positive (velocity strengthening), a fault slips stably, whereas a fault has the potential to nucleate an earthquake when ($a-b$) is negative (velocity weakening).

3.4. Microstructures

Polished sections of the post-experiment samples were prepared after impregnating the samples with epoxy resin and cutting normal to the gouge and parallel to the shear direction. Microstructures of the gouge were observed by a scanning electron microscope (SEM, Hitachi SU-3500) at Geological Survey of Japan, using the backscattered electron (BSE) mode. We used the energy dispersive spectroscopy (EDS) analysis as well to identify mineral phases.

4. Results

Experiments at high temperature and higher effective pressure conditions showed higher differential stresses (Figure 3a). We observed slip-dependent trends of friction coefficient that are negative at lower temperature-pressure conditions and positive at higher temperature-pressure conditions (Figure 3b). During the displacement interval with V_{axial} of 0.01 μm/s, pore fluid was continuously expelled from the gouge (Figure 2b), suggesting that the axial deformation was partly consumed by the compaction of the gouge. The gouge thickness remained almost constant at the other velocity conditions as the pore fluid volume kept almost constant. Moreover, systematic fluctuations in friction data were observed in all experiments when V_{axial} was 0.01 μm/s. The phases of the fluctuation recorded on the external load cell and on the internal load cell were lagged by ~100 seconds, and fluctuations occurred at every ~1000 seconds regardless of experimental conditions (Figure S2). In addition, the fluctuations occurred even when the ($a-b$) values were positive; therefore, the fluctuations at V_{axial} of 0.01 μm/s were not stick-slip behavior of gouge but stick-slips at an O-ring at the hydraulic actuator pushing up the vessel or around the compensation chamber (Figure S1). We therefore consider that the data obtained at V_{axial} of 0.01 μm/s will not represent mechanical properties for shear deformation.

We used steady-state friction coefficients (μ) at V_{axial} = 1 μm/s for representative values of each run: 0.13-0.22 for 30% illite in S/I mixture, 0.16-0.21 for 50% illite, 0.24-0.26 for 70% illite, 0.36 for 90% illite, and 0.41-0.43 for 95% illite (Figure 3c). The ($a-b$) values ranged from 0.0026 to 0.0057 for 30% illite (T = 55°C), from 0.0008 to 0.0038 for 50% illite (T = 104°C), from 0.0013 to 0.0045 for 70% illite (T = 118°C), from 0.0016 to 0.0050 for 90% illite (T = 150°C), and from −0.0032 to 0.0042 for illite 95% illite (T = 171°C) (Figure 4a). As the friction data at V_{axial} of 0.01 μm/s may be influenced by the compaction behavior of gouge and a noise from the O-ring at a hydraulic actuator, we only determined the RSF parameters at the velocities over 0.1 μm/s. Negative ($a-b$) values were observed only at low velocity conditions (<1.15 to 11.55 μm/s) of the run HTP1133 with 95% illite. Little systematic variation in d_c was observed among velocity and experimental conditions (Figure 4b), whereas both a and b increased with increasing illite content (i.e., simultaneously increasing temperature and pressure) at all velocity conditions (Figures 4c and d).

In the microstructures 12or all five experiments, non-clay mineral (quartz, albite, and orthoclase) grains are dispersed within the S/I mixture, and few instances of discernable shear plane are observed (Figure 5). Non-clay mineral grains appear to be more fragmented for the samples which underwent the higher effective stress and temperature conditions. These features may indicate that the shear deformation is basically distributed within the S/I mixture, but non-clay mineral grains partly accommodated deformation.

5. Discussion

5.1. Spatial variation in frictional strength

Before interpreting the effect of the S/I transition in friction coefficient (μ), we firstly calibrate the quartz and illite contents. Since the illite sample may contain ~10% of quartz, quartz and illite contents could be slightly over- and underestimated, respectively, especially for the cases of higher temperature conditions that contained more illite. For HTP1133 (simulating 95% illite in the S/I mixture) for example, the actual quartz content is 25.7% and illite is 51.3% in the gouge assuming that 10% of the illite is actually quartz. Nevertheless, the illite content in the S/I mixture is 94.5% in this case. Therefore, quartz and illite contents in the gouge can be varied by ~6% at most, whereas the illite content in the S/I mixture is influenced only by ~0.5% at most. Since the purpose of this study is to understand the role of the S/I transition in frictional properties, we consider that our experimentations were insignificantly affected by the quartz contamination in the illite sample under an appropriate treatment on the overestimated quartz content. In the following discussion, we accordingly corrected the quartz content within the gouge.

Previous studies showed that μ for pure smectite and pure illite under room temperature are ~0.1 and ~0.3, respectively (Mizutani et al., 2017; Morrow et al., 2017; Takahashi et al., 2007; Tembe et al., 2010). Effective pressure and pore pressure have little effects on μ of illite gouge (Ikari et al., 2009; Moore et al., 1989; Morrow et al., 1992). The μ for smectite gouge may increase with effective normal stress (Mizutani et al., 2017; Morrow et al., 2017) whereas its sensitivity to pore pressure is minor (Morrow et al., 2017). Smectite shows a weak decreasing trend of μ from 0.1 to 0.05 as temperature (T) increases from room temperature to 150 °C, especially at low effective normal stress conditions (Mizutani et al., 2017). In contrast, μ for illite shows a increasing trend with T: μ at 200 °C is about 0.35 (den Hartog et al., 2012) to 0.49 (Moore et al., 1989). Note that μ can be varied with slip (den Hartog et al., 2012) or foliations of fault rocks (Tesei et al., 2015), although we will not take those effects into account in this study. For non-clay minerals (quartz, albite, orthoclase), they generally follow the Byerlee's rule (Byerlee, 1978; Morrow et al., 2000).

Based on the abovementioned μ values for each mineral phase, we found that the Reuss average (equation 7) well-explains the friction coefficient for mixed gouges in this study rather than the Voigt average (equation 8) (Figure 3c). The most plausible μ_m was 0.71 for non-clay minerals, 0.08 for smectite, and 0.38 for illite in this study, which are consistent with typical values for those materials. The Voigt average provided higher bulk friction coefficients with the same combination of μ_m than the Reuss average and experimental data (Figure 3c). As all grains are subjected to identical stress for the system with the Reuss average, the weaker S/I mixture accommodates more shear strain than stronger non-clay mineral grains. The microstructures which the non-clay mineral grains are dispersed within the S/I matrix (Figure 5) are consistent with the feature that is expected from the Reuss average.

Assuming that the Reuss average (equation 7) controls the variation in μ along the décollement, the spatial distribution of the S/I mixture (Figure 1c) can be recast into the spatial pattern of friction coefficient. The obtained μ showed a landward increasing trend such that it is 0.16-0.35 beneath the outer prism and 0.35-0.44 beneath the inner prism along the plate boundary zone (Figure 6b). Such a landward increasing trend of friction coefficient was also inferred by the Coulomb wedge model combining the prism topography with frictional strength of core samples from the accretionary prism, which did not include any *a priori* mineralogical variations (Okuda et al., 2021). They proposed that the μ at the trench-ward portion along the plate boundary beneath the outer prism is 0.24 (Ikari et al., 2013), and that the μ increases to 0.5-0.6 near the boundary between the outer and inner prisms, and to 0.6-0.8 at the updip limit depth of seismogenic zone. Although the results in this study at the trench-ward portion are consistent with the previous studies, the friction coefficient we obtained were lower than that predicted in the Coulomb wedge model.

5.2. Inference on pore pressure condition

The discrepancy in the estimated friction coefficient (μ) along the plate boundary may be due to difference in the assumptions of pore pressure conditions adopted in the Coulomb wedge model. P-wave velocity (Kitajima & Saffer, 2012; Tsuji et al., 2014) and hydrological modeling (Saffer & Bekins, 1998; Screaton et al., 1990; Skarbek & Saffer, 2009) have been used to estimate pore pressure conditions around the plate boundary. In the Nankai Trough, the plate boundary zone is thought to be over-pressured having a pore pressure ratio λ along the décollement of the Kumano transect, defined by the ratio between pore pressure and lithostatic overburden (Saffer & Tobin, 2011), of 0.84 to 0.95 in Tsuji et al. (2014) and 0.73 to 0.86 in Kitajima & Saffer (2012). Based on these studies, the previous study (Okuda et al., 2021) assumed the λ along the bottom of accretionary prism (=λ_b) to be 0.5 beneath the prism toe, 0.7 at the trench-ward part beneath the outer prism, 0.9 at the landward part beneath the outer prism, and 0.8 beneath the inner prism. Nearly hydrostatic pore pressure conditions were assumed inside the prism (λ = 0.5). As the Coulomb wedge model predicts a higher μ for a higher λ_b, the discrepancy in the absolute values of μ along the plate boundary could be originated from the uncertainty in pore pressure conditions assumed in the Coulomb wedge model.

To anticipate the pore pressure conditions along the plate boundary from the experimental series in this study, we tested two endmembers of plate boundary condition based on previous interpretations of the depth of décollement (Figure 6a): (A) the prism is supported by the roof of underthrust sediment (β (dip angle) = 0° at the outer prism and 10.1° at the inner prism, dashed line in Figure 6) (Shiraishi et al., 2020; Tsuji et al., 2014), and (B) the prism is supported by the bottom of underthrust sediment (β = 3.5° at the outer prism and 7° at the inner prism, solid line in Figure 6) (Hüpers et al., 2019; Moore et al., 2009). The slope angles of seafloor (α) are 4° and 0.1° for the outer and inner prisms. The μ of sediment within the outer prism (μ_w) was assumed to be 0.30-0.55 and that within the inner prism was 0.45-0.60 based on friction studies on the drilled samples from each prism (Fujioka et al., 2022; Okuda et al., 2021). From those μ values along the underthrust sediment and the prism sediments, the λ_b can be evaluated by following equations of the Coulomb wedge model (Dahlen, 1990):

$$(1-\lambda_b)\mu_b = (1-\lambda_w)\tan\phi_b\,, \tag{11}$$

where ϕ_b satisfies the following equation:

$$\frac{1}{2}\arcsin\left(\frac{\sin\phi_b}{\sin\phi}\right) - \frac{1}{2}\phi_b = \alpha + \beta + \frac{1}{2}\arcsin\left(\frac{\sin\alpha'}{\sin\phi}\right) - \frac{1}{2}\alpha', \tag{12}$$

where ϕ and α' are defined as:

$$\mu_w = \tan\phi\,, \tag{13}$$

$$\tan\alpha' = \left(\frac{1-\rho_w/\rho}{1-\lambda_w}\right)\tan\alpha\,, \tag{14}$$

where ρ and ρ_w are the densities of prism sediment (2.2 g/cm^3) and seawater (1.024 g/cm^3). The pore pressure ratios within the outer and inner prisms (λ_w) were assumed to be nearly hydrostatic (λ_w = 0.5) (Akuhara et al., 2020; Kitajima et al., 2017). We disregard the boundary area between the outer and inner prism because of its complex geological structure such as a splay fault branching from the décollement.

The estimated λ_b values are summarized in Figure 6c: 0.61-0.74 (case A, μ_w = 0.30), 0.48-0.66 (case B, μ_w = 0.30), 0.38-0.60 (case A, μ_w = 0.55), 0.08-0.40 (case B, μ_w = 0.55) beneath the outer prism, and 0.66-0.73 (case A, μ_w = 0.45), 0.75-0.81 (case B, μ_w = 0.45), 0.49-0.60 (case A, μ_w = 0.60), 0.63-0.71 (case B, μ_w = 0.60) beneath the inner prism. Those results are lower than those estimated from P-wave velocity and hydrological modeling studies (λ_b = 0.73-0.95). As the assumed stress state in conversion of P-wave velocity to pore pressures (Kitajima & Saffer, 2012; Tsuji et al., 2014), permeability (Screaton et al., 1990), or rate of compaction of underthrust sediment (Saffer & Bekins, 1998) may change the pore pressure estimation, we expect that the pore pressure conditions of underthrust sediment may be overestimated due to the uncertainties in such parameters. However, diagenetic processes such as lithification potentially increase the frictional strength of underthrust sediment (Ikari & Hüpers, 2021). In such a case, near lithostatic pore pressure could be sustained by high (frictional) strength of underthrust sediment as estimated in previous studies (Okuda et al., 2021). Especially beneath the outer prism area, the pore pressure ratio was estimated to be lower than hydrostatic pore pressure for μ_w = 0.55 (Figure 6c). This situation is improbable as the plate boundary area in subduction zone should be saturated with fluid, although such a situation can be avoided if μ_w = 0.30. Nevertheless, effects of diagenetic processes on frictional strength of sediment would be needed to be evaluated toward precise understanding of pore pressure and mechanical conditions along the plate boundary area.

5.3. Implications for seismic activities in the shallow Nankai Trough

In this study, we only observed velocity (*V*)-weakening behavior, which is requisite for a potential of nucleating an earthquake, in the case of the sample with 95% illite in S/I mixture at 171 °C with less than ~10 μm/s (Figure 4a). Only *V* strengthening was observed at less than 30 km distance from the trough axis (Figure 7b), where the S/I conversion has already completed (Figure 7a). Previous studies reported that illite-rich shale showed positive ($a-b$) values at <200 °C (den Hartog et al., 2012; Phillips et al., 2020) and smectite is also *V* strengthening up to 150 °C (Mizutani et al., 2017). For smectite, ($a-b$) decreases with effective normal stress of up to 70 MPa (Mizutani et al., 2017; Morrow et al., 2017). Sediment samples from the Nankai Trough and illite-rich shale showed a positive trend on ($a-b$) with respect to a reduction in effective normal stress and an increase in pore pressure (Bedford et al., 2021; Fujioka et al., 2022; den Hartog & Spiers, 2013). All those studies suggest that sediments may be frictionally stable at the *in-situ* temperature-pressure-mineral conditions in the shallow part of the Nankai accretionary prism. Granite and altered basalt show negative ($a-b$) values, but they have higher friction coefficients than sediment in general (Blanpied et al., 1995; Okuda et al., 2023; Phillips et al., 2020). Therefore, on the scheme of the RSF law, the underthrust sediment would not have the potential to nucleate an earthquake beneath the outer prism.

However, shallow slow earthquakes such as very low frequency earthquakes

(Takemura, Obara, et al., 2022) and slow slip events (Yokota & Ishikawa, 2020) have been observed along the shallow plate boundary area in the Nankai Trough (Figure 7c). If shallow slow earthquakes are a consequence of unstable slip in the V-weakening system, sediment within the underthrust sequence must undergo some processes that make the sediment V weakening, such as lithification (Ikari & Hüpers, 2021; Roesner et al., 2020) or having a small-scale material heterogeneity of patches of V weakening and strengthening (Bedford et al., 2022). Another possibility is that the frictional strength is apparently reduced due to fluid pressurization with slip associated with the impermeable nature of clay-rich sediment (Faulkner et al., 2018). The potential linkage between fluid migration and shallow slow earthquakes in the Nankai Trough (Tonegawa et al., 2022) could have interpretations on the mechanism of shallow slow earthquakes where classical frictional instability described by the RSF law may not be applicable for the nucleation process of shallow slow earthquakes.

The temperature condition of 171 °C where negative ($a-b$) values were observed at <10 μm/s may correspond to the transition from aseismic to seismic along the décollement. Practically, the 2016 Off-Mie earthquake occurred at around 40 to 50 km landward from the trough axis (Nakano et al., 2018; Wallace et al., 2016), close to the updip limit of the seismogenic zone (Figure 7c). As the smectite-illite transition mostly completed at 30 km from the trough axis (Figure 7a), the transition from V strengthening to weakening may not be governed by the smectite-illite transition as opposed to the hypothesis in previous studies (Hyndman et al., 1997). Previous experiments on illite-rich shale found the transition from V-strengthening to V-weakening for 1-100 μm/s at around 200-250 °C (den Hartog et al., 2012; den Hartog & Spiers, 2013). As they mentioned that the V range of V weakening will shift to lower V

conditions at a lower temperature condition, the observed negative ($a-b$) values at 171 °C with <10 μm/s in this study may originate from the temperature dependence of ($a-b$) of illite-rich sediment. Consequently, the updip limit depth of the seismogenic zone is primarily controlled by temperature-dependent frictional behavior of illite-rich sediment rather than by the S/I transition (den Hartog & Spiers, 2013). As the T range of negative ($a-b$) shifts to lower temperature range with increasing quartz fraction (den Hartog et al., 2014), the depth of the updip limit of the seismogenic zone can be variable when the quartz fraction is spatially varied due to variations in origin of sediments, for example. It is worth noting that the transition from negative to positive ($a-b$) values at ~10 μm/s may lead to slow slip event as a rupture propagation can be interrupted by stable slip (Shibazaki & Iio, 2003). Such transition may result in an area where both slow earthquakes (e.g., slow slip event) and regular events (e.g., the 2016 Off-Mie earthquake) could occur.

6. Conclusion

We conducted friction experiments on simulated fault gouge under *in-situ* temperature-pressure-mineral conditions along the plate boundary zone at the Kumano transect in the Nankai trough. Friction coefficient increased landward from 0.16 at the trough axis to 0.44 at 50 km landward from the trough axis with increasing illite content, following the Reuss average of friction coefficients of non-clay minerals (quartz, albite, and orthoclase), smectite, and illite. The gouge exhibited velocity strengthening (positive ($a-b$) value) at up to the temperature of 150 °C (~30 km from the trough axis), whereas the gouge becomes velocity weakening at 171 °C at low (<10 μm/s) velocity conditions. Since the smectite-illite transition mostly completed at ~30 km from the trough axis, the experimental results indicate that the smectite-illite transition does not play a role in the transition from velocity strengthening to velocity weakening, but temperature-dependent frictional behavior of illite-rich materials may govern the updip limit of the seismogenic zone of a subduction zone. Based on the friction coefficients obtained in this study, we inferred that pore pressure conditions within the underthrust sediment may be over-pressured but not close to lithostatic, although diagenetic processes may increase friction coefficient of sediments, which eventually sustains high pore pressure conditions. The obtained velocity strengthening behavior of sediment in the most regions in the Nankai Trough suggest that other possibilities such as lithification processes, a small-scale heterogeneity, or apparent reduction in friction by fluid pressurization may be required for the generations of the shallow slow earthquakes.

Acknowledgements

Samples and experimental assemblies were partly provided by Norio Shigematsu (GSJ), Wataru Tanikawa (JAMSTEC), and Keishi Okazaki (Hiroshima University). This work benefited from KAKENHI grants (JP20J20413 to H. Okuda; JP19H04621, JP21H01189, and JP21H05202 to A. Yamaguchi).

References

Akuhara, T., Tsuji, T., & Tonegawa, T. (2020). Overpressured Underthrust Sediment in the Nankai Trough Forearc Inferred From Transdimensional Inversion of High-Frequency Teleseismic Waveforms. *Geophysical Research Letters, 47*(15). https://doi.org/10.1029/2020GL088280

Ando, M. (1975). Source mechanisms and tectonic significance of historical earthquakes along the nankai trough, Japan. *Tectonophysics, 27*(2), 119–140. https://doi.org/10.1016/0040-1951(75)90102-X

Araki, E., Saffer, D. M., Kopf, A. J., Wallace, L. M., Kimura, T., Machida, Y., et al. (2017). Recurring and triggered slow-slip events near the trench at the Nankai Trough subduction megathrust. *Science*, *356*(6343), 1157–1160. https://doi.org/10.1126/science.aan3120

Ariyoshi, K., Iinuma, T., Nakano, M., Kimura, T., Araki, E., Machida, Y., et al. (2021). Characteristics of Slow Slip Event in March 2020 Revealed From Borehole and DONET Observatories. *Frontiers in Earth Science*, *8*(January), 1–15. https://doi.org/10.3389/feart.2020.600793

Bedford, J. D., Faulkner, D. R., Allen, M. J., & Hirose, T. (2021). The stabilizing effect of high pore-fluid pressure along subduction megathrust faults: Evidence from friction experiments on accretionary sediments from the Nankai Trough. *Earth and Planetary Science Letters*, *574*, 117161. https://doi.org/10.1016/j.epsl.2021.117161

Bedford, J. D., Faulkner, D. R., & Lapusta, N. (2022). Fault rock heterogeneity can produce fault weakness and reduce fault stability. *Nature Communications*, *13*(1), 326. https://doi.org/10.1038/s41467-022-27998-2

Blanpied, M. L., Lockner, D. A., & Byerlee, J. D. (1995). Frictional slip of granite at hydrothermal conditions. *Journal of Geophysical Research: Solid Earth*, *100*(B7), 13045–13064. https://doi.org/10.1029/95JB00862

Blanpied, M. L., Marone, C., Lockner, D. A., Byerlee, J. D., & King, D. P. (1998). Quantitative measure of the variation in fault rheology due to fluid-rock interactions. *Journal of Geophysical Research: Solid Earth*, *103*(B5), 9691–9712.

https://doi.org/10.1029/98JB00162

Byerlee, J. D. (1978). Friction of rocks. *Pure and Applied Geophysics PAGEOPH, 116*(4–5), 615–626. https://doi.org/10.1007/BF00876528

Dahlen, F. A. (1990). Critical Taper Model of Fold-And-Thrust Belts and Accretionary Wedges. *Annual Review of Earth and Planetary Sciences*, *18*(1), 55–99. https://doi.org/10.1146/annurev.ea.18.050190.000415

den Hartog, S. A. M., & Spiers, C. J. (2013). Influence of subduction zone conditions and gouge composition on frictional slip stability of megathrust faults. *Tectonophysics*, *600*, 75–90. https://doi.org/10.1016/j.tecto.2012.11.006

den Hartog, S. A. M., Niemeijer, A. R., & Spiers, C. J. (2012). New constraints on megathrust slip stability under subduction zone P – T conditions. *Earth and Planetary Science Letters*, *353–354*, 240–252. https://doi.org/10.1016/j.epsl.2012.08.022

den Hartog, S. A. M., Saffer, D. M., & Spiers, C. J. (2014). The roles of quartz and water in controlling unstable slip in phyllosilicate-rich megathrust fault gouges. *Earth, Planets and Space*, *66*(1), 78. https://doi.org/10.1186/1880-5981-66-78

Dieterich, J. H. (1979). Modeling of rock friction: 1. Experimental results and constitutive equations. *Journal of Geophysical Research*, *84*(B5), 2161. https://doi.org/10.1029/JB084iB05p02161

Faulkner, D. R., Sánchez-Roa, C., Boulton, C., den Hartog, S. A. M., Sanchez-Roa, C., Boulton, C., & den Hartog, S. A. M. (2018). Pore Fluid Pressure Development in Compacting Fault Gouge in Theory, Experiments, and Nature. *Journal of Geophysical Research: Solid Earth*, *123*(1), 226–241. https://doi.org/10.1002/2017JB015130

Fujioka, R., Katayama, I., Kitamura, M., Okuda, H., & Hirose, T. (2022). Depth profile of frictional properties in the inner Nankai accretionary prism using cuttings from IODP Site C0002. *Progress in Earth and Planetary Science*, *9*(1), 31. https://doi.org/10.1186/s40645-022-00488-1

Garrett, E., Fujiwara, O., Garrett, P., Heyvaert, V. M. A., Shishikura, M., Yokoyama, Y., et al. (2016). A systematic review of geological evidence for Holocene earthquakes and tsunamis along the Nankai-Suruga Trough, Japan. *Earth-Science Reviews*, *159*, 337–357. https://doi.org/10.1016/j.earscirev.2016.06.011

Hüpers, A., Grathoff, G., Warr, L. N., Wemmer, K., Spinelli, G. A., & Underwood, M. B. (2019). Spatiotemporal Characterization of Smectite-to-Illite Diagenesis in the Nankai Trough Accretionary Prism Revealed by Samples From 3 km Below Seafloor. *Geochemistry, Geophysics, Geosystems*, *20*(2), 933–951. https://doi.org/10.1029/2018GC008015

Hyndman, R. D., Yamano, M., & Oleskevich, D. A. (1997). The seismogenic zone of subduction thrust faults. *The Island Arc*, *6*(3), 244–260. https://doi.org/10.1111/j.1440-1738.1997.tb00175.x

Ikari, M. J., & Hüpers, A. (2021). Velocity-weakening friction induced by laboratory-controlled lithification. *Earth and Planetary Science Letters*, *554*, 116682. https://doi.org/10.1016/j.epsl.2020.116682

Ikari, M. J., Saffer, D. M., & Marone, C. (2009). Frictional and hydrologic properties of clay-rich fault gouge. *Journal of Geophysical Research*, *114*(B5), B05409. https://doi.org/10.1029/2008JB006089

Ikari, M. J., Hüpers, A., & Kopf, A. J. (2013). Shear strength of sediments approaching subduction in the Nankai Trough, Japan as constraints on forearc mechanics.

Geochemistry, Geophysics, Geosystems, *14*(8), 2716–2730. https://doi.org/10.1002/ggge.20156

Kitajima, H., & Saffer, D. M. (2012). Elevated pore pressure and anomalously low stress in regions of low frequency earthquakes along the Nankai Trough subduction megathrust. *Geophysical Research Letters*, *39*(23), n/a-n/a. https://doi.org/10.1029/2012GL053793

Kitajima, H., Saffer, D. M., Sone, H., Tobin, H. J., & Hirose, T. (2017). In Situ Stress and Pore Pressure in the Deep Interior of the Nankai Accretionary Prism, Integrated Ocean Drilling Program Site C0002. *Geophysical Research Letters*, *44*(19), 9644–9652. https://doi.org/10.1002/2017GL075127

Kubo, T., & Katayama, I. (2015). Effect of temperature on the frictional behavior of smectite and illite. *Journal of Mineralogical and Petrological Sciences, 110*(6), 293–299. https://doi.org/10.2465/jmps.150421

Masuda, K., Fujimoto, K., & Arai, T. (2002). A new gas-medium, high-pressure and high-temperature deformation apparatus at AIST, Japan. *Earth, Planets and Space*, *54*(11), 1091–1094. https://doi.org/10.1186/BF03353307

Mizutani, T., Hirauchi, K., Lin, W., & Sawai, M. (2017). Depth dependence of the frictional behavior of montmorillonite fault gouge: Implications for seismicity along a décollement zone. *Geophysical Research Letters*, *44*(11), 5383–5390. https://doi.org/10.1002/2017GL073465

Moore, D. E., & Lockner, D. A. (2011). Frictional strengths of talc-serpentine and talc-quartz mixtures. *Journal of Geophysical Research, 116*(B1), B01403. https://doi.org/10.1029/2010JB007881

Moore, D. E., Summers, R., & Byerlee, J. D. (1989). Sliding behavior and deformation textures of heated illite gouge. *Journal of Structural Geology*, *11*(3), 329–342. https://doi.org/10.1016/0191-8141(89)90072-2

Moore, G. F., Park, J.-O., Bangs, N. L., Gulick, S. P., Tobin, H. J., Nakamura, Y., et al. (2009). Structural and seismic stratigraphic framework of the NanTroSEIZE Stage 1 transect. In *Proceedings of the Integrated Ocean Drilling Program* (Vol. 314). https://doi.org/10.2204/iodp.proc.314315316.102.2009

Morrow, C. A., Radney, B., & Byerlee, J. D. (1992). Frictional Strength and the Effective Pressure Law of Montmorillonite and lllite Clays. *International Geophysics*, *51*(C), 69–88. https://doi.org/10.1016/S0074-6142(08)62815-6

Morrow, C. A., Moore, D. E., & Lockner, D. A. (2000). The effect of mineral bond strength and adsorbed water on fault gouge frictional strength. *Geophysical Research Letters*, *27*(6), 815–818. https://doi.org/10.1029/1999GL008401

Morrow, C. A., Moore, D. E., & Lockner, D. A. (2017). Frictional strength of wet and dry montmorillonite. *Journal of Geophysical Research: Solid Earth*, *122*(5), 3392–3409. https://doi.org/10.1002/2016JB013658

Nakano, M., Hyodo, M., Nakanishi, A., Yamashita, M., Hori, T., Kamiya, S., et al. (2018). The 2016 Mw 5.9 earthquake off the southeastern coast of Mie Prefecture as an indicator of preparatory processes of the next Nankai Trough megathrust earthquake. *Progress in Earth and Planetary Science*, *5*(1), 30. https://doi.org/10.1186/s40645-018-0188-3

Noda, H., & Takahashi, M. (2016). Correction of output from an internal load cell in a high-pressure triaxial deformation apparatus without a split-piston. *The Journal of the Geological Society of Japan*, *122*(12), 653–658. https://doi.org/10.5575/geosoc.2016.0047

Okuda, H., Ikari, M. J., Roesner, A., Stanislowski, K., Hüpers, A., Yamaguchi, A., & Kopf, A. J. (2021). Spatial Patterns in Frictional Behavior of Sediments Along the Kumano Transect in the Nankai Trough. *Journal of Geophysical Research: Solid Earth*, *126*(11). https://doi.org/10.1029/2021JB022546

Okuda, H., Niemeijer, A. R., Takahashi, M., Yamaguchi, A., & Spiers, C. J. (2023). Hydrothermal Friction Experiments on Simulated Basaltic Fault Gouge and Implications for Megathrust Earthquakes. *Journal of Geophysical Research: Solid Earth*, *128*(1). https://doi.org/10.1029/2022JB025072

Phillips, N. J., Belzer, B., French, M. E., Rowe, C. D., & Ujiie, K. (2020). Frictional Strengths of Subduction Thrust Rocks in the Region of Shallow Slow Earthquakes. *Journal of Geophysical Research: Solid Earth*, *125*(3), 1–20. https://doi.org/10.1029/2019JB018888

Pytte, A. M., & Reynolds, R. C. (1989). The thermal transformation of Smectite to Illite. In *Thermal History of Sedimentary Basins*.

Roesner, A., Ikari, M. J., Saffer, D. M., Stanislowski, K., Eijsink, A. M., & Kopf, A. J. (2020). Friction experiments under in-situ stress reveal unexpected velocity-weakening in Nankai accretionary prism samples. *Earth and Planetary Science Letters*, *538*, 116180. https://doi.org/10.1016/j.epsl.2020.116180

Ruina, A. L. (1983). Slip instability and state variable friction laws. *Journal of Geophysical Research: Solid Earth*, *88*(B12), 10359–10370. https://doi.org/10.1029/JB088iB12p10359

Saffer, D. M., & Bekins, B. A. (1998). Episodic fluid flow in the Nankai accretionary complex: Timescale, geochemistry, flow rates, and fluid budget. *Journal of Geophysical Research: Solid Earth*, *103*(B12), 30351–30370.

https://doi.org/10.1029/98JB01983

Saffer, D. M., & Marone, C. (2003). Comparison of smectite- and illite-rich gouge frictional properties: application to the updip limit of the seismogenic zone along subduction megathrusts. *Earth and Planetary Science Letters*, *215*(1–2), 219–235. https://doi.org/10.1016/S0012-821X(03)00424-2

Saffer, D. M., & Tobin, H. J. (2011). Hydrogeology and Mechanics of Subduction Zone Forearcs: Fluid Flow and Pore Pressure. *Annual Review of Earth and Planetary Sciences*, *39*(1), 157–186. https://doi.org/10.1146/annurev-earth-040610-133408

Saffer, D. M., Lockner, D. A., & McKiernan, A. W. (2012). Effects of smectite to illite transformation on the frictional strength and sliding stability of intact marine mudstones. *Geophysical Research Letters*, *39*(11), L11304. https://doi.org/10.1029/2012GL051761

Screaton, E. J., Wuthrich, D. R., & Dreiss, S. J. (1990). Permeabilities, fluid pressures, and flow rates in the Barbados Ridge Complex. *Journal of Geophysical Research*, *95*(B6), 8997. https://doi.org/10.1029/JB095iB06p08997

Shibazaki, B., & Iio, Y. (2003). On the physical mechanism of silent slip events along the deeper part of the seismogenic zone. *Geophysical Research Letters*, *30*(9), 1489. https://doi.org/10.1029/2003GL017047

Skarbek, R. M., & Saffer, D. M. (2009). Pore pressure development beneath the décollement at the Nankai subduction zone: Implications for plate boundary fault strength and sediment dewatering. *Journal of Geophysical Research: Solid Earth*, *114*(7), 1–20. https://doi.org/10.1029/2008JB006205

Sugihara, T., Kinoshita, M., Araki, E., Kimura, T., Kyo, M., Namba, Y., et al. (2014). Re-evaluation of temperature at the updip limit of locked portion of Nankai megasplay inferred from IODP Site C0002 temperature observatory New Perspective of Subduction Zone Earthquake. *Earth, Planets and Space*, *66*(1), 577–590. https://doi.org/10.1186/1880-5981-66-107

Sugioka, H., Okamoto, T., Nakamura, T., Ishihara, Y., Ito, A., Obana, K., et al. (2012). Tsunamigenic potential of the shallow subduction plate boundary inferred from slow seismic slip. *Nature Geoscience*, *5*(6), 414–418. https://doi.org/10.1038/ngeo1466

Takahashi, M., Mizoguchi, K., Kitamura, K., & Masuda, K. (2007). Effects of clay content on the frictional strength and fluid transport property of faults. *Journal of Geophysical Research*, *112*(B8), B08206. https://doi.org/10.1029/2006JB004678

Takemura, S., Baba, S., Yabe, S., Emoto, K., Shiomi, K., & Matsuzawa, T. (2022). Source Characteristics and Along-Strike Variations of Shallow Very Low Frequency Earthquake Swarms on the Nankai Trough Shallow Plate Boundary. *Geophysical Research Letters*, *49*(11). https://doi.org/10.1029/2022GL097979

Takemura, S., Obara, K., Shiomi, K., & Baba, S. (2022). Spatiotemporal Variations of Shallow Very Low Frequency Earthquake Activity Southeast Off the Kii Peninsula, Along the Nankai Trough, Japan. *Journal of Geophysical Research: Solid Earth*, *127*(3). https://doi.org/10.1029/2021JB023073

Tembe, S., Lockner, D. A., & Wong, T.-F. (2010). Effect of clay content and mineralogy on frictional sliding behavior of simulated gouges: Binary and ternary mixtures of quartz, illite, and montmorillonite. *Journal of Geophysical Research*, *115*(B3), B03416. https://doi.org/10.1029/2009JB006383

Tesei, T., Lacroix, B., & Collettini, C. (2015). Fault strength in thin-skinned tectonic wedges across the smectite-illite transition: Constraints from friction experiments and critical tapers. *Geology*, *43*(10), 923–926. https://doi.org/10.1130/G36978.1

Tobin, H. J., Hirose, T., Saffer, D. M., Toczko, S., Maeda, L., Kubo, Y., et al. (2015). Site C0002. In *Proceedings of the Integrated Ocean Drilling Program* (Vol. 348). https://doi.org/10.2204/iodp.proc.348.103.2015

Tonegawa, T., Takemura, S., Yabe, S., & Yomogida, K. (2022). Fluid Migration Before and During Slow Earthquakes in the Shallow Nankai Subduction Zone. *Journal of Geophysical Research: Solid Earth*, *127*(3), 1–15. https://doi.org/10.1029/2021JB023583

Tsuji, T., Kamei, R., & Pratt, R. G. (2014). Pore pressure distribution of a mega-splay fault system in the Nankai Trough subduction zone: Insight into up-dip extent of the seismogenic zone. *Earth and Planetary Science Letters*, *396*, 165–178. https://doi.org/10.1016/j.epsl.2014.04.011

Underwood, M. B., & Song, C. (2016). Data report: clay mineral assemblages in cores from Hole C0002P, IODP Expedition 348, Nankai Trough accretionary prism. In *Proceedings of the Integrated Ocean Drilling Program* (Vol. 348, pp. 1–13). https://doi.org/10.2204/iodp.proc.348.202.2016

Vrolijk, P. (1990). On the mechanical role of smectite in subduction zones. *Geology*, *18*(8), 703. https://doi.org/10.1130/0091-7613(1990)018<0703:OTMROS>2.3.CO;2

Wallace, L. M., Araki, E., Saffer, D., Wang, X., Roesner, A., Kopf, A., et al. (2016). Near-field observations of an offshore M w 6.0 earthquake from an integrated seafloor and subseafloor monitoring network at the Nankai Trough, southwest Japan. *Journal of Geophysical Research: Solid Earth*, *121*(11), 8338–8351. https://doi.org/10.1002/2016JB013417

Yokota, Y., & Ishikawa, T. (2020). Shallow slow slip events along the Nankai Trough detected by GNSS-A. *Science Advances*, *6*(3), eaay5786. https://doi.org/10.1126/sciadv.aay5786

Table 1. Summary of experimental conditions. P_c: confining pressure, P_f: pore pressure, P_{eff}: effective pressure, T: temperature.

Run	P_c [MPa]	P_f [MPa]	P_{eff} [MPa]	T [°C]	Illite in S/I mixture [%]
HTP1129	73.4	28.6 → 57.3	44.8 → 16.1	55	30
HTP1130	100.1	32.5 → 65.0	67.6 → 35.1	104	50
HTP1134	110.0	33.9 → 67.8	76.1 → 42.2	118	70
HTP1132	134.8	37.5 → 75.0	97.3 → 59.8	150	90
HTP1133	160.7	42.9 → 85.7	117.8 → 75.0	171	95

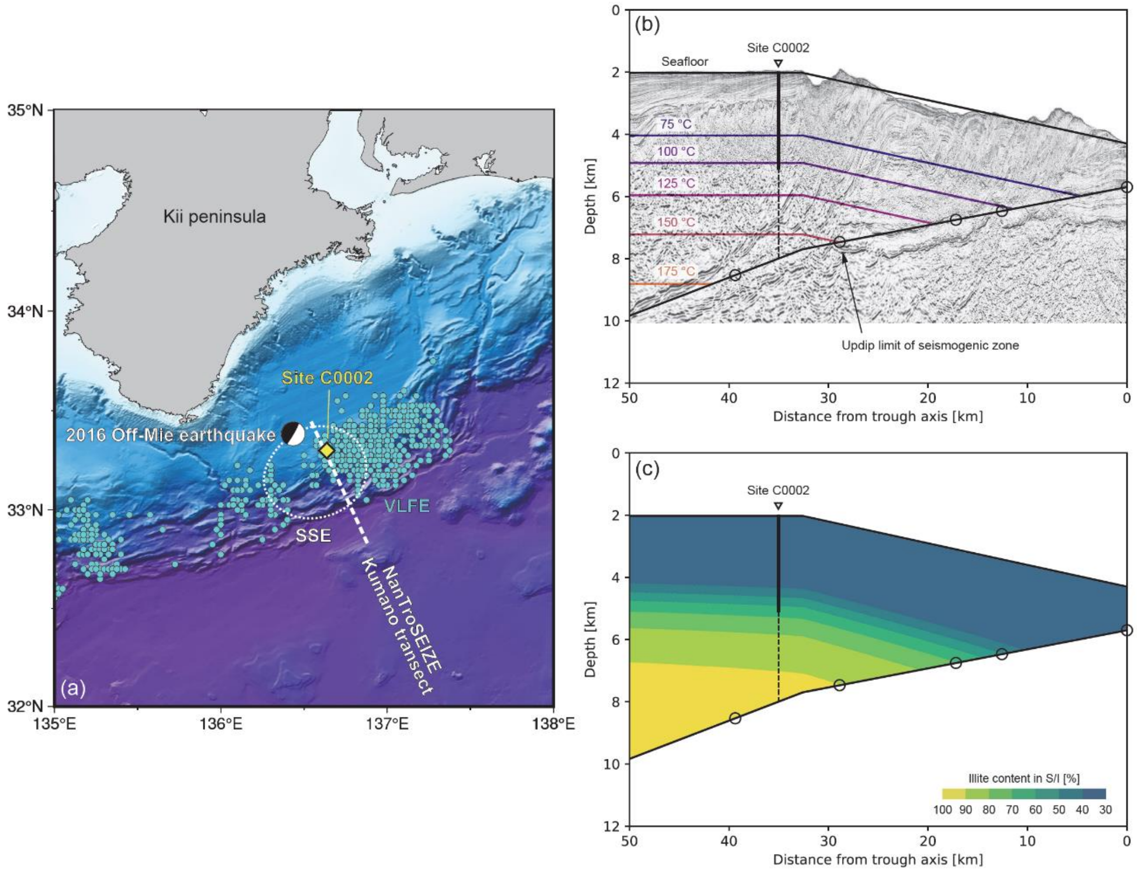

Figure 1. (a) Map of the off-Kumano Nankai Trough. Hypocenters of very low frequency earthquake (VLFE) (Takemura, Baba, et al., 2022; Takemura, Obara, et al., 2022), the slip area of a slow slip event (SSE) (Yokota & Ishikawa, 2020), the hypocenter of 2016 Off-Mie earthquake (Wallace et al., 2016), and locations of the Kumano transect and Site C0002 are shown. (b) Simplified geometry used in this study with the seismic reflection profile along the Kumano transect in the Nankai Trough (G. F. Moore et al., 2009). The location of Site C0002 is also indicated. Circles represent the locations tested in this study. Temperature conditions are also shown (Sugihara et al., 2014). (c) Distribution of illite content in S/I mixture (Hüpers et al., 2019).

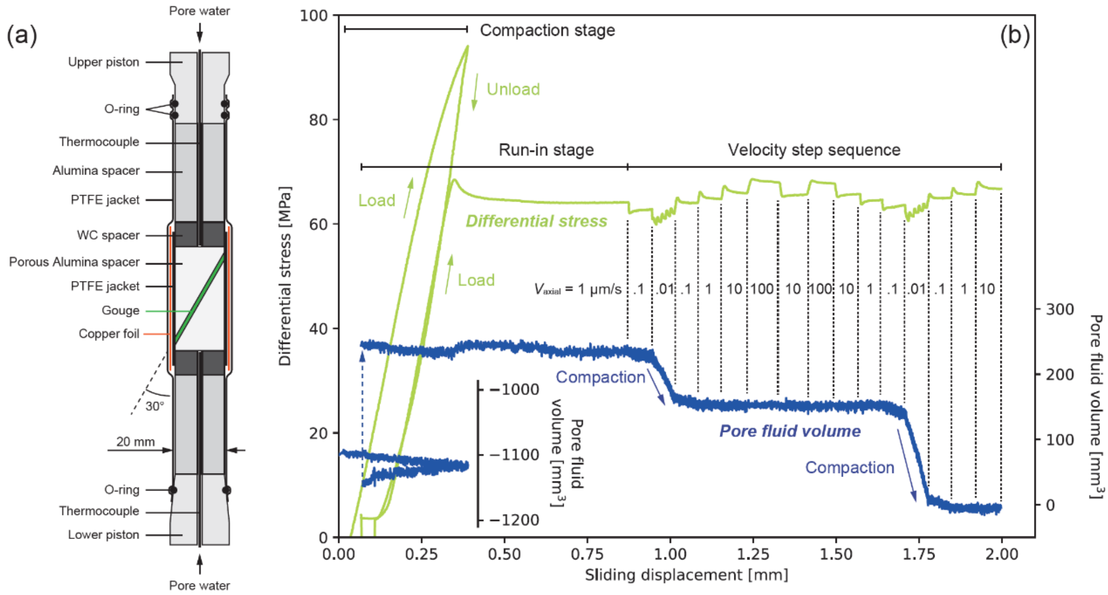

Figure 2. (a) Schematic view of the sample assembly. (b) Experimental procedure and measured differential stress (HTP1132, T = 150 °C, P_c = 134.8 MPa, P_f = 37.5 during the compaction stage and 75.0 MPa during the run-in stage and velocity step sequence). Pore fluid volume measured at the pore pressure intensifier is also shown by blue line.

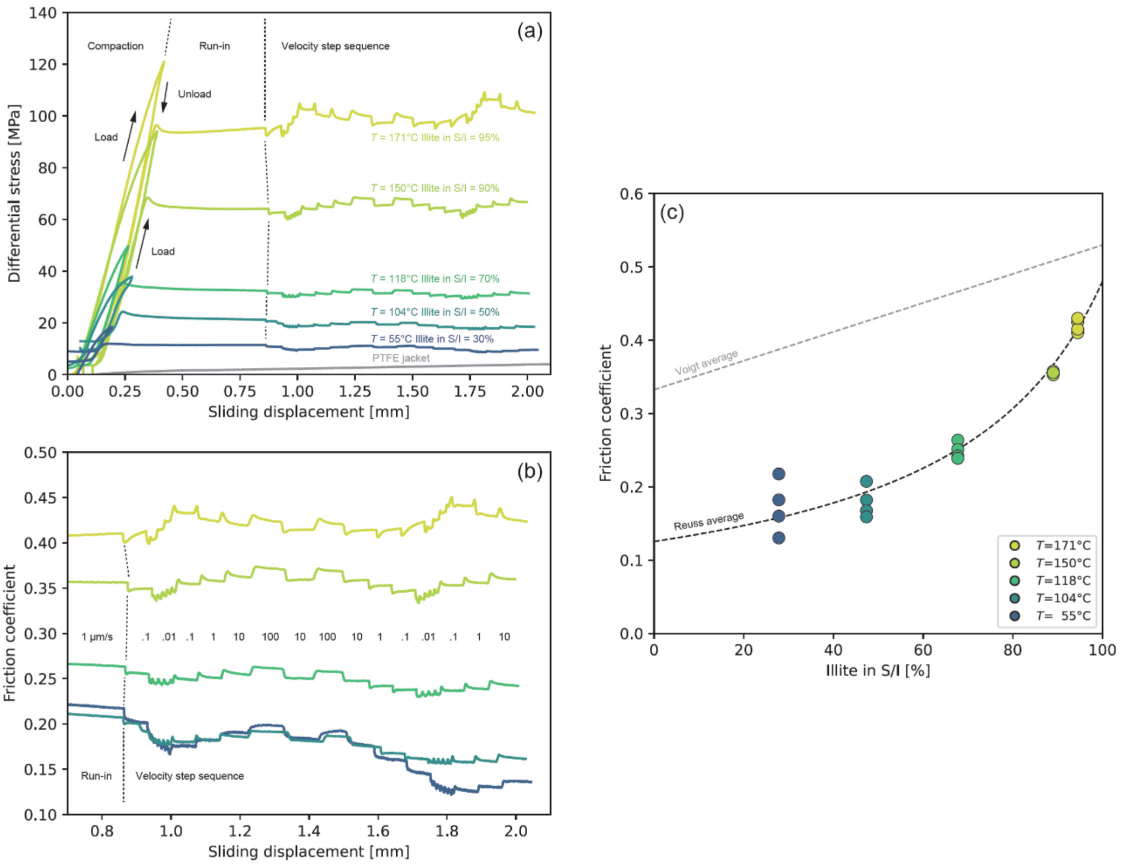

Figure 3. (a) Curves of differential stress for all experiments. (b) Friction coefficients at run-in and velocity step sequence after removing the jacket effect. (c) Friction coefficients at the axial velocity of 1 μm/s. Dashed lines represent the Reuss and Voigt averages with the friction coefficient for smectite of 0.08, that for illite of 0.38, and that for non-clay minerals of 0.71.

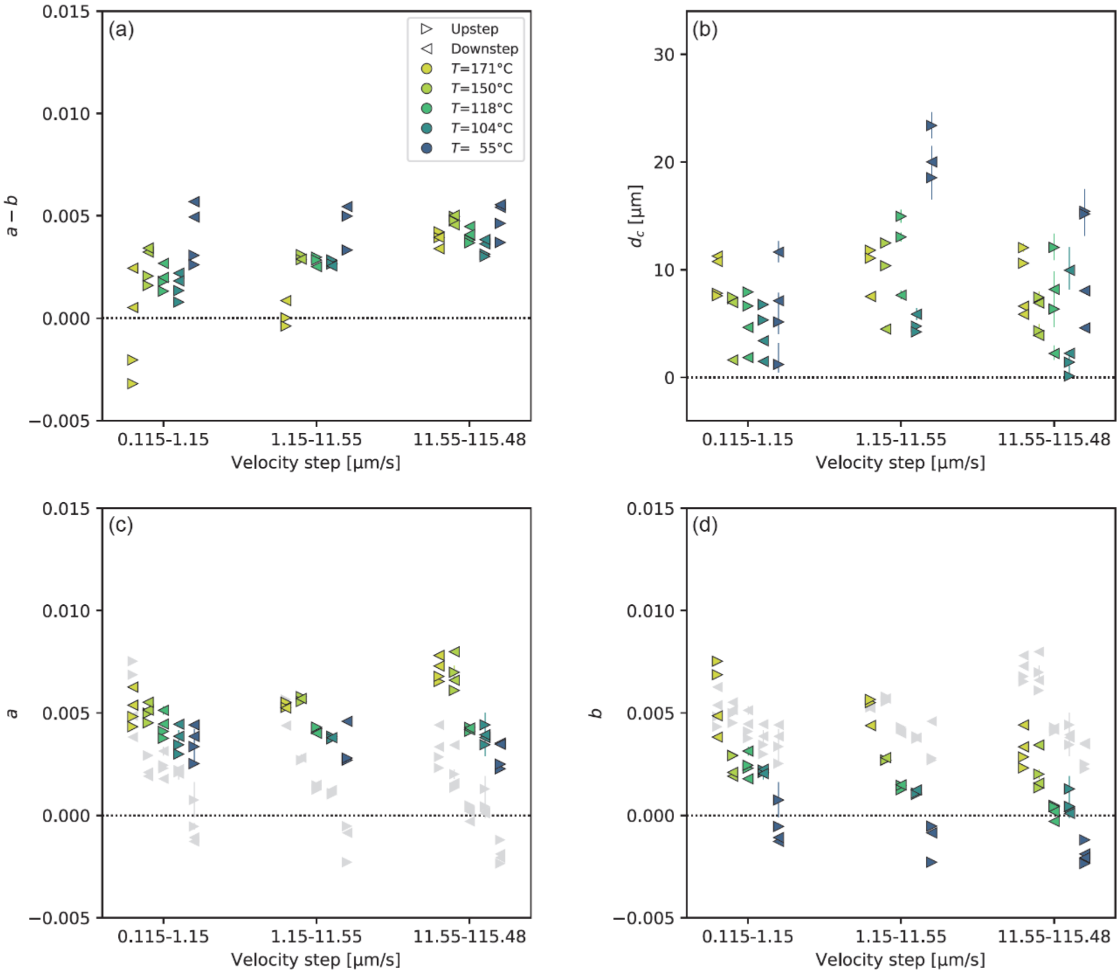

Figure 4. (a) The parameter $(a-b)$ for the rate- and state-dependent friction (RSF) law. The parameters d_c, a, and b are shown in (b), (c), and (d), respectively. Gray markers in (c) and (d) are the b and a values for comparison.

737

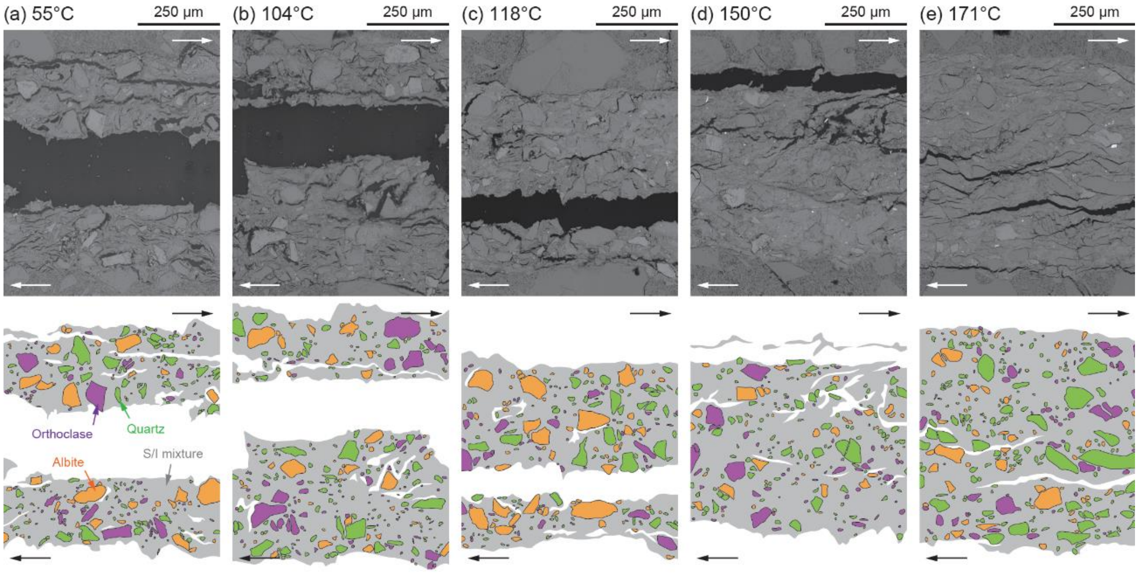

738 **Figure 5.** Microstructures of the post-experiment samples. Lower panels are sketches of
739 the distribution of each mineral phase (gray: smectite-illite (S/I) mixture; green: quartz;
740 orange: albite; purple: orthoclase).

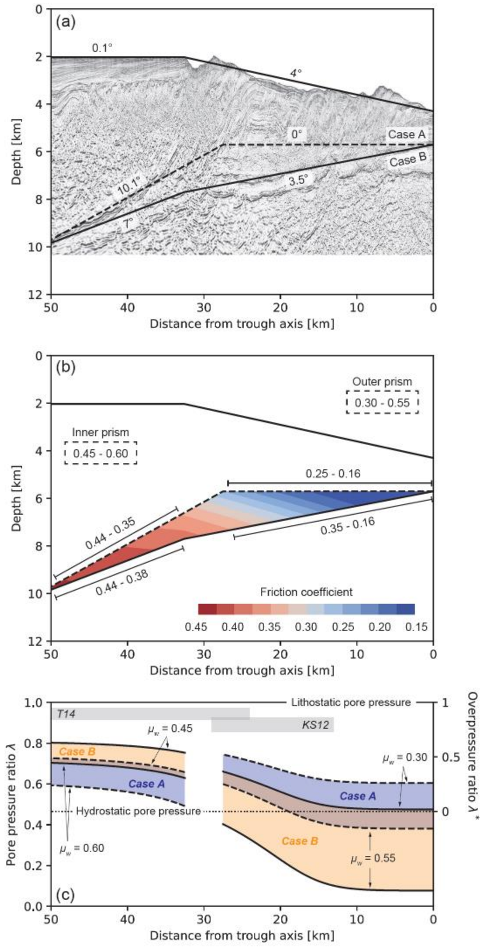

Figure 6. (a) Assumed geometry along the Kumano transect for the Coulomb wedge modeling. (b) Variation in friction coefficient within the underthrust sequence calculated from the S/I distribution (Figure 1b) and the Reuss average of friction coefficients (μ = 0.71 for non-clay minerals, 0.08 for smectite, and 0.38 for illite). Assumed friction coefficients for sediments within the outer and inner prisms are also shown (Fujioka et al., 2022; Okuda et al., 2021). (c) Estimated pore pressure ratio along the plate boundary (λ_b) calculated from the geometry (a) and μ (b). Gray areas are the pore pressure conditions along the Nankai Trough estimated from P-wave velocity (KS12: Kitajima & Saffer, 2012; T14: Tsuji et al., 2014).

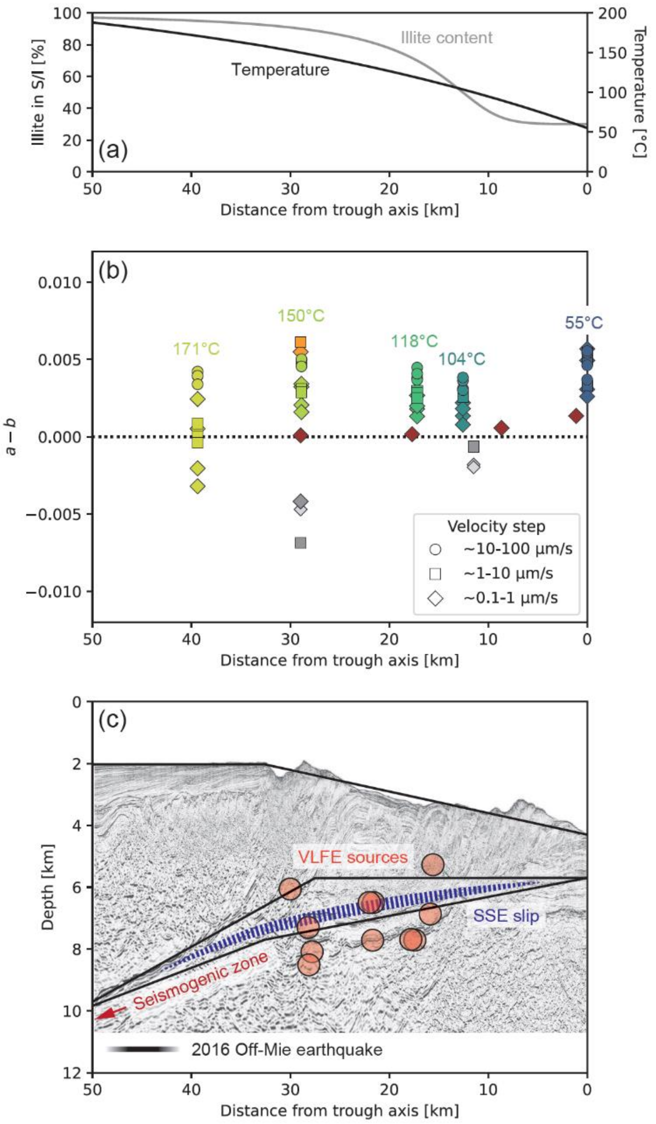

Figure 7. (a) Temperature condition (black line) and illite content (gray line) along the underthrust sediment. (b) Variation in ($a-b$) values based on temperature conditions at various locations along the bottom of accretionary prism. Brown markers: smectite (Mizutani et al., 2017); light gray markers: granite (Blanpied et al., 1995, 1998); orange markers: illite-rich shale (den Hartog et al., 2012; Phillips et al., 2020); gray markers: altered basalt (Okuda et al., 2023; Phillips et al., 2020). (c) Locations of very low frequency earthquakes (VLFE), slow slip events (SSE) (Araki et al., 2017; Ariyoshi et al., 2021; Sugioka et al., 2012), and 2016 Off-Mie earthquake (Nakano et al., 2018;

Wallace et al., 2016) in the shallow Nankai Trough.